Check for updates

Chemistry – A European Journal

ChemEurJ Chemistry Europe European Chemical Societies Publishing

RESEARCH ARTICLE OPEN ACCESS

Three-Step Synthesis Toward Fluorene-Based Non-Fused-Ring Acceptors for Organic Solar Cells

Virginia Lafranconi[1] | Suman Mallick[1] | Lisa Nauta[1] | Lisa Inzko[1] | Julia Hönigsberger[1] | Danijel Babic[1] | Bettina Schlemmer[1] | Daniele Padula[2] | Heinz Amenitsch[3] | Thomas Rath[1] | Gregor Trimmel[1]

[1]Institute for Chemistry and Technology of Materials (ICTM), NAWI Graz, Graz University of Technology, Graz, Austria | [2]Dipartimento di Biotecnologie, Chimica e Farmacia, Università di Siena, Siena, Italy | [3]Institute of Inorganic Chemistry, NAWI Graz, Graz University of Technology, Graz, Austria

Correspondence: Gregor Trimmel (gregor.trimmel@tugraz.at)

Received: 23 January 2026 | **Revised:** 4 March 2026 | **Accepted:** 17 March 2026

Keywords: fluorene | non-fullerene electron acceptors | organic solar cells | synthesis design | thermal stability | thin films

ABSTRACT

Non-fused-ring electron acceptors have recently gathered substantial interest for the application in organic solar cells because of their competitive photovoltaic properties and other advantages, including easy synthesis and high yields, facilitating the production of cost-efficient devices. In this work, a pair of fluorene-based acceptors, FHM-Cl and FHM-F, respectively featuring a chlorinated and a fluorinated 1,1-dicyanomethylene-3-indanone end group, π-bridged through alkyl-substituted thiophene units to a fluorene core, were synthesized through a three-step synthesis from commercially available precursors. Organic solar cells utilizing these acceptor molecules were subsequently fabricated and optimized with various donor materials. Notably, the combinations D18:FHM-Cl and D18:FHM-F achieved power conversion efficiencies of 10.7% and 7.6%, respectively. A comprehensive study involving optical and electrical characterization, along with morphological analysis, demonstrated that the FHM-Cl-based solar cells exhibited superior light absorption, enhanced solid-state packing and reduced trap-assisted recombination. Moreover, the shelf and thermal stability of the devices further highlight the potential of these acceptors in the design of low-cost and efficient organic solar cells.

1 | Introduction

Organic solar cells (OSCs) have attracted significant attention due to their numerous advantages, including low production costs, lightweight, semi-transparency, inherent mechanical flexibility, and compatibility with roll-to-roll manufacturing, making them highly adaptable energy conversion solutions [1–3]. Recent progress in molecular design and synthesis of high-performance organic photovoltaic materials has resulted in a remarkable enhancement of power conversion efficiency (PCE) in OSCs. Notably, the advent of non-fullerene electron acceptors featuring an acceptor–donor–acceptor (A–D–A) fused-ring architecture has pushed PCEs beyond the 20% benchmark in single-junction devices [4–7]. Despite the improvement achieved with Y6 and its derivatives, fused-ring electron acceptors (FREAs) continue to suffer from complex, multistep synthetic routes and low-yield ring-closure reactions, which substantially challenge OSCs' large-scale production and commercialization [8, 9]. To address these limitations, the development of non-fused-ring electron acceptors (NFREAs) has emerged as a promising alternative approach [10–12]. NFREAs simplify the conventional fused-ring architectures by substituting the rigid polycyclic frameworks with simpler three-ring or mono-/bi-cyclic units connected through single σ-bonds. Typically, NFREA molecules adopt an A–π–D–π–A configuration, in which the D core can comprise a substituted phenyl moiety such as 2,5-difluorobenzene, as well as Si-, N-, or C-bridged bithiophene or indenothiophene groups, the π-bridges are often based on thienyl or benzothiadiazole derivatives,

This is an open access article under the terms of the Creative Commons Attribution-NonCommercial License, which permits use, distribution and reproduction in any medium, provided the original work is properly cited and is not used for commercial purposes.

© 2026 The Author(s). *Chemistry – A European Journal* published by Wiley-VCH GmbH

and the terminal units are electron-withdrawing groups that facilitate efficient intramolecular charge transfer [13, 14]. From a molecular design perspective, core engineering is a tool to tune energy levels and optoelectronic characteristics through systematic conjugated backbone modification. Substituent engineering enables noncovalent intermolecular interactions and molecular packing via functional or steric group manipulation, thereby suppressing intramolecular bond rotation between the aromatic rings and promoting the extended conjugation length, crucial for optimal optoelectronic properties in OPV materials [15–18]. One method adopted by Zhang et al. is modulating the size, number, and position of lateral alkyl chains on the π-bridge to effectively promote molecular stacking, achieving a PCE of 14.2% [19]. Ding et al. implemented a dipole-oriented molecular design by leveraging polarization from multiple orientations of terminal chlorine atoms on the alkyl chains. This approach induced the formation of a locked-in-cavity crystal structure, which enhanced charge transfer and transport while stabilizing the blend morphology, ultimately achieving NFREA OSCs with a PCE of 16.9% [20]. Recent studies have demonstrated that regulating peripheral substituents to encapsulate the central bithiophene core, enforces a more planar conformation, significantly enhancing the device performance [21, 22]. Through this strategy, a record-breaking PCE of 18.0% was achieved by Wang et al., greatly narrowing the efficiency gap between NFREAs and FREAs [23].

Among various donor core moieties, only a few studies have explored the use of low-cost fluorene as a promising building block for the design of novel NFREAs [24–27]. In 2015, Holliday et al. [25] reported FBR, a fluorene-based NFREA incorporating a benzothiadiazole unit to extend π-conjugation end-capped with a rhodamine derivative as the electron-withdrawing end group. In 2018, Zhang et al. [27] further optimized this design by introducing thiophene π-bridges and employing the brominated derivative of the well-established end group 1,1-dicyanomethylene-3-indanone, yielding F8IDT-Br. The corresponding PM6:F8IDT-Br based devices achieved a maximum PCE of nearly 10% and exhibited good shelf-life stability, while the thermal stability was limited.

Indeed, end-group halogenation is as an effective approach to develop high-performance acceptors, as the strong electron-withdrawing nature of halogen substituents enhances the push–pull interaction between the D core and the A unit. Fluorination and chlorination represent the most extensively explored halogenation strategies reported in the literature [9, 28–30]. Owing to their high electronegativity, both halogens induce effective intramolecular redistribution of electron density, leading to a downshift of the frontier molecular orbital energy levels as well as a modulation of the absorption spectra. Fluorine, characterized by the highest electronegativity and a small atomic radius, facilitates specific intra- and intermolecular noncovalent interactions (F···H and F···S), thereby influencing molecular conformation and solid-state packing. In contrast, chlorine substitution, despite introducing increased steric hindrance due to its larger atomic radius, can promote π-electron delocalization due to its higher polarizability, thereby strengthening intramolecular charge-transfer characteristics [31, 32].

Inspired by these studies, we synthesized two A–π–D–π–A -type NFREAs **FHM-Cl** (2,2′-((2Z,2′Z)-(((9,9-dioctyl-9H-fluorene-2,7-diyl)bis(3-hexylthiophene-5,2-diyl))bis(methaneylylidene))bis(5,6-dichloro-3-oxo-2,3-dihydro-1H-indene-2,1-diylidene))dimalononitrile) and **FHM-F** (2,2′-((2Z,2′Z)-(((9,9-dioctyl-9H-fluorene-2,7-diyl)bis(3-hexylthiophene-5,2-diyl))bis(methaneylylidene))bis(5,6-difluoro-3-oxo-2,3-dihydro-1H-indene-2,1-diylidene))dimalononitrile), via a concise three-step synthetic route starting from commercially available precursors. In our molecular design, the fluorene core was selected to facilitate charge transport and maintain conjugation along the molecular backbone, while alkyl-substituted thiophene units were employed as π-bridges. The incorporation of alkyl substituents at the β-positions of the thiophene rings enhances molecular planarity through steric effects, which suppress torsional rotation around single σ-bonds and promote stronger intermolecular interactions, thereby improving charge transport properties and conformational stability [10, 33, 34]. In this work, we present a direct comparison between chlorinated FHM-Cl and fluorinated FHM-F to investigate the influence of halogen substitution on the intrinsic optoelectronic and photovoltaic properties [32, 35]. When blended with the donor D18, the corresponding devices achieved PCEs of 10.7% and 7.6% for FHM-Cl and FHM-F, respectively, remarkable values considering the concise three-step synthesis of these NFREAs. Both devices exhibited good thermal stability, with the FHM-F and FHM-Cl based devices showing respectively 15% and 25% efficiency loss after 950 h of prolonged thermal aging.

2 | Results and Discussion

2.1 | Synthesis and Characterization

A three-step synthesis route, shown in Scheme 1, leads to the final compounds FHM-F and FHM-Cl with an overall yield of 51% and 40%, respectively. At first, a Suzuki coupling reaction was carried out to introduce thiophene groups to both sides of a fluorene core using $Pd(PPh_3)_4$ as catalyst and K_2CO_3 as base. After purification using column chromatography, a yield of 77% and 74% was achieved.

In the second step, compound **2** was reacted with DMF and $POCl_3$ in a Vilsmeier–Haack reaction, leading to the introduction of an aldehyde group on the thiophene rings. After column chromatography, yields of 79% and 68% were obtained [36]. Finally, a Knoevenagel condensation reaction with pyridine as catalyst was performed with compound **3**, resulting in the attachment of the end groups to the molecule. Column chromatography followed by recrystallisation from dichloromethane/hexane was used for purification. The final compounds, FHM-F and FHM-Cl, were obtained as dark blue shimmering solid and the structures were confirmed by NMR spectroscopy and mass spectrometry (see Supporting Information Sections 1.2, 1.3, and 1.4). Yields of 86% and 67% were achieved for the last step, significantly higher than the 58% reported in the literature [27].

2.2 | Physical Properties

To assess the physical properties of FHM-F and FHM-Cl, UV–vis absorption spectroscopy and cyclic voltammetry measurements were performed. The results are summarized in Table 1.

15213765, 0, Downloaded from https://chemistry-europe.onlinelibrary.wiley.com/doi/10.1002/chem.70952 by CochraneItalia, Wiley Online Library on [09/04/2026]. See the Terms and Conditions (https://onlinelibrary.wiley.com/terms-and-conditions) on Wiley Online Library for rules of use; OA articles are governed by the applicable Creative Commons License

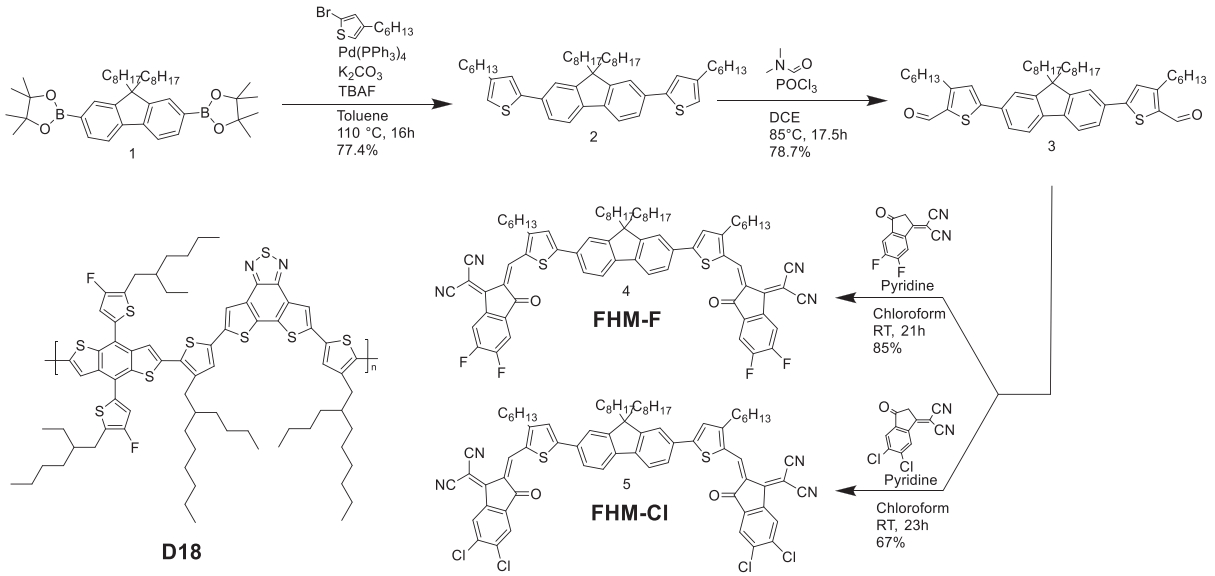

SCHEME 1 | Synthetic route toward the FHM-F and FHM-Cl non-fullerene acceptors and the chemical structure of D18.

TABLE 1 | Optical and electronic properties of FHM-Cl and FHM-F.

	Solution			Thin film		Cyclic voltammetry		
	λ_{max} [nm]	E_g [eV]	ε [$M^{-1}cm^{-1}$]	λ_{max} [nm]	E_g [eV]	HOMO [eV]	LUMO [eV]	E_g [eV]
FHM-Cl	623	1.83	$2.09 \cdot 10^5$	663	1.70	−6.44	−4.52	1.92
FHM-F	609	1.88	$1.96 \cdot 10^5$	646	1.74	−6.54	−4.52	2.02

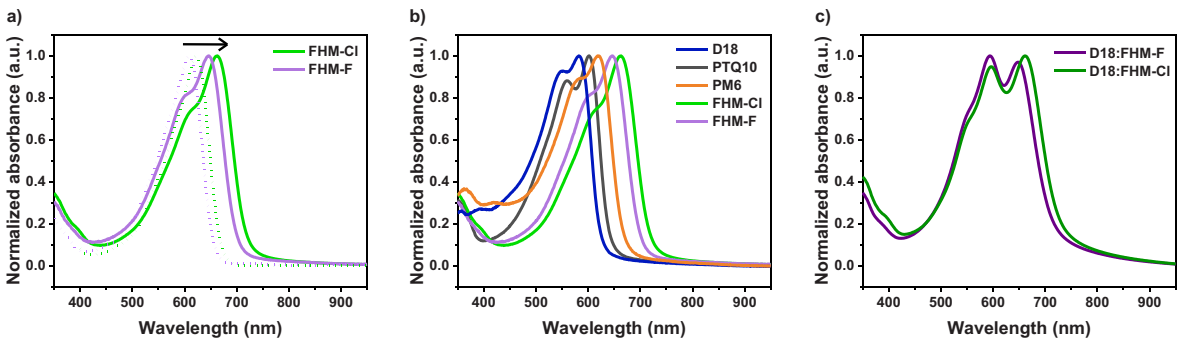

FIGURE 1 | Optical properties: (a) normalized UV−vis absorption spectra in $CHCl_3$ (dashed) and thin film (solid) spectra; (b) normalized UV–vis absorption thin film spectra of the tested donors and the novel acceptors; (c) normalized thin film absorption of D18:FHM-F and D18:FHM-Cl blends.

The UV–vis absorption spectra of both acceptors in solution and thin films are shown in Figure 1a. The maximum absorption occurs at 609 nm for FHM-F and 623 nm for FHM-Cl in $CHCl_3$ solution, and at 643 and 663 nm in thin films, respectively. Therefore, the absorption spectrum of FHM-F exhibits a blue shift relative to that of the chlorinated analogue, FHM-Cl. Both, the solid-state spectra display a clear red shift resulting from an ordered intermolecular packing, where the presence of a shoulder indicates the formation of aggregate species and π–π interactions in the thin film. The shift is greater in the case of FHM-F indicating a more compact arrangement probably due to the smaller radius of the fluorine atom. The slightly higher absorption coefficient (ε) observed in $CHCl_3$ solution for FHM-Cl (2.09×10^5 M^{-1} cm^{-1}) indicates a stronger light-harvesting capacity compared to FHM-F (1.96×10^5 M^{-1} cm^{-1}). This phenomenon is mainly attributed to the higher dipole moment and oscillator strength of the C–Cl bond relative to the C–F bond [32].

The frontier molecular orbital energies were determined by cyclic voltammetry using the oxidation/reduction onset potentials (see Supporting Information 2.2, Figure S15). The highest occupied

15213765, 0, Downloaded from https://chemistry-europe.onlinelibrary.wiley.com/doi/10.1002/chem.70952 by CochraneItalia, Wiley Online Library on [09/04/2026]. See the Terms and Conditions (https://onlinelibrary.wiley.com/terms-and-conditions) on Wiley Online Library for rules of use; OA articles are governed by the applicable Creative Commons License

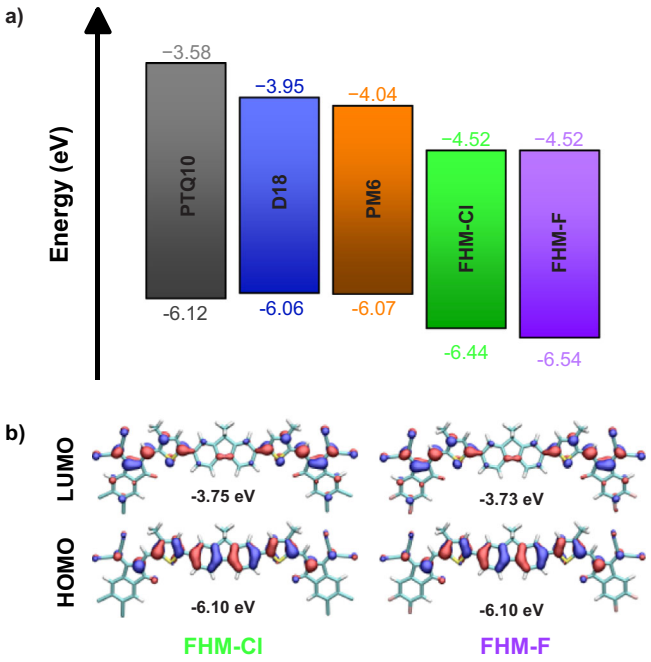

FIGURE 2 | (a) Frontier molecular orbital energies determined by cyclic voltammetry and energy level alignment of donors and acceptors; (b) DFT-calculated frontier molecular orbitals.

molecular orbital (HOMO) energy levels of FHM-F and FHM-Cl were found to be −6.54 and −6.44 eV, while the lowest unoccupied molecular orbital (LUMO) energy levels were quantified as −4.52 eV for both acceptors (Figure 2a). In general, halogenation effectively tunes the energy levels of organic semiconductors, with fluorination typically lowering the HOMO energy level more than chlorination, as observed in our case. This is because the electronegative nature of fluorine can enhance the overall electron-withdrawing capacity of the substituent, thus lowering the orbital energies, which is crucial for facilitating better electron acceptance from donor materials [37].

DFT (density functional theory) and TDDFT (time-dependent density functional theory) calculations were carried out to have a deeper understanding of the structural packing through reorganization energy. Specifically, the B3LYP-D3BJ/def2-TZVP method was used for the geometry optimization and TDDFT/M06-2X/def2-TZVPP was employed for assessing optical and electronic properties of FHM-Cl and FHM-F. The DFT-calculated frontier molecular orbitals and their energies are shown in Figure 2b. The hexyl chains in the FHM structures were cropped to methyl chains, as commonly reported in the literature [38]. Tables S1 and S2 report computational results, which are consistent with experimental optical and electronic findings, whereas discrepancies between values derived from CV measurements and computed DFT ones are due to solvent effects and redox kinetics mechanisms [39]. Solvation in CV measured energies results deeper HOMO/LUMO levels compared to vacuum DFT orbitals [40]. Moreover, donor and acceptor electrostatic potential (ESP) distributions are displayed in Figure S3a–c, illustrating a positive ESP in the central backbone among the fluorene core and thiophenes for FHM acceptors. Conversely, the electronegative groups, such as fluorine and chlorine, as well as the carbonyl and cyano groups, show negative ESP.

Moreover, we computationally evaluated the geometry twist imposed by the fluorene unit, the most probable arrangements between pairs of acceptor molecules, as well as the electron transfer integral between them. The computational strategy adopted is described in the Supporting Information (Section 2.3), along with the torsional energy profile (Figure S14), the structures of the most strongly interacting dimers (in terms of their interaction energies) and transfer integrals (see Table S3). Although the fluorene unit introduces a modest twist (∼18°) with the adjacent thiophenes, the low torsional barrier allows access to nearly planar conformations, which are further stabilized in the condensed phase by enhanced conjugation and π–π stacking interactions. The transfer integrals govern charge transfer: the higher the value, the better the transport. The most stable arrangement for FHM-Cl (−76.2 kJ mol^{-1}) has a higher transfer integral (33 meV) than the most stable arrangement for FHM-F (−96.7 kJ mol^{-1}, 21 meV). The reorganization energy is found to be slightly smaller for FHM-Cl (131 meV) compared to FHM-F (140 meV).

Overall, FHM-Cl is indicated to be a better acceptor, according to these results, owing to its lower reorganization energy and higher transfer integral in the dimer with the strongest interaction energy.

2.3 | Surface Energy and Miscibility

Three different polymers, PTQ10, PM6, and D18, (Figure S16 and Scheme 1) were considered as promising donors in blend with the acceptors FHM-F and FHM-Cl. The evaluation was carried out based on their complementarity of the absorption spectra (Figure 1b), alignment of the frontier molecular orbital energies (Figure 2b), as well as the suitability of the surface free energy.

The morphological behavior of donors and acceptors in blend films is related to their miscibility. Two materials with a low interfacial energy value could reduce the energetic penalty required to create a well−mixed interpenetrating network of donors and acceptors with a large interfacial area [41]. Contact angle (CA) measurements [42] of thin films with water and diiodomethane (DIM) as test liquids were performed (see Supporting Information 2.4 and Figure S17). The Wu method was used to determine surface free energy values [43] and, consequently, the interfacial energies between donor and acceptor components were calculated according to the Flory–Huggins model and summarized in Table S4. The similar CA values indicate that the PM6 and D18 donors reveal comparable surface energy (γ) values (γ_{D18} = 35.1 mN m^{-1}, γ_{PM6} = 35.8 mN m^{-1}), whereas PTQ10 exhibits a weaker surface interaction (31.3 mN m^{-1}). Considering the neat acceptor films, FHM-F (38.10 mN m^{-1}), displays a lower γ value compared to FHM-Cl (44.1 mN m^{-1}). The Flory–Huggins model quantifies the blend miscibility within two components through the interaction parameters (χ), given the equation: $\chi = (\gamma_{donor}^{1/2} - \gamma_{acceptor}^{1/2})^2$. Extreme miscibility, associated with a very small χ value, can lead to impure phase domains and detrimental charge recombination, whereas an excessively large χ value may cause pronounced phase separation. Therefore, a moderate χ value is essential for optimizing the morphology of the blend film [41]. The χ values between FHM-F and PTQ10/PM6/D18 (0.33/0.036/0.062) are one order of magnitude [41] smaller than the values between FHM-Cl and

15213765, 0, Downloaded from https://chemistry-europe.onlinelibrary.wiley.com/doi/10.1002/chem.70952 by CochraneItalia, Wiley Online Library on [09/04/2026]. See the Terms and Conditions (https://onlinelibrary.wiley.com/terms-and-conditions) on Wiley Online Library for rules of use; OA articles are governed by the applicable Creative Commons License

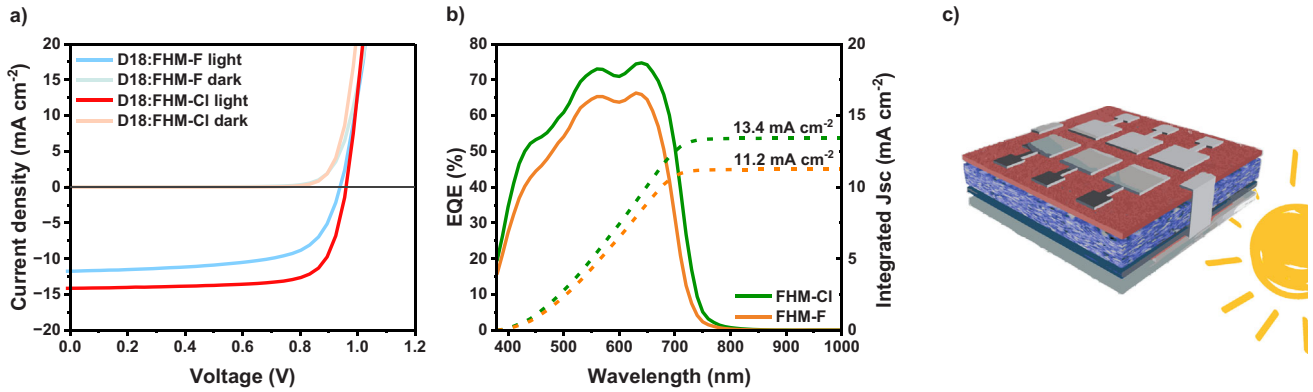

FIGURE 3 | Photovoltaic performance: *J–V* curves of (a) D18:FHM-Cl and D18:FHM-F based solar cells in dark and illuminated conditions; (b) EQE curves from the corresponding best devices; (c) scheme of the fabricated solar cells in conventional device architecture.

TABLE 2 | Absorber layer thickness and photovoltaic parameters of D18:FHM based solar cells under 100 mW cm^{-2} illumination with a spectrum similar to AM 1.5 G.

	Thickness [nm]	V_{oc} [V]	J_{sc} [mA cm^{-2}]	FF	PCE[a] [%]	Best PCE [%]	R_s [ohm cm^2]	J_{calc}[b] [mA cm^{-2}]
D18:FHM-Cl	75 ± 4	0.95 ± 0.01	13.85 ± 0.84	0.73 ± 0.03	9.59 ± 0.78	10.69	3.08	13.4
D18:FHM-F	73 ± 5	0.94 ± 0.01	11.80 ± 0.62	0.63 ± 0.02	6.99 ± 0.38	7.64	6.14	11.2

[a]Average values obtained from more than 12 devices.
[b]Calculated J_{sc} values obtained from the EQE spectra.

PTQ10/PM6/D18 (1.10/0.44/0.52). It appears that substituting the F atoms with Cl atoms on the end-groups can increase the surface tension difference and reduce the miscibility between donors and acceptors, resulting in an increased phase-separation degree, which is beneficial for higher domain purity [44] in PM6 and D18 blends, consistently with the device characterization in the following section.

2.4 | Properties of FHM-F and FHM-Cl Based Solar Cells

To evaluate the photovoltaic performance of the synthesized acceptor materials, OSCs in the conventional architecture glass/ITO/PEDOT:PSS/donor:acceptor/PDINN/Ag were fabricated (Figure 3c). FHM-Cl and FHM-F are tested as acceptor compounds with the three donors PTQ10, PM6, and D18, by varying concentration and ratio of the D:A solution. The detailed procedures for fabricating the OSCs (Sections 2.7 and 2.8) as well as the photovoltaic parameters of these screening experiments (Figures S18 and S19 and Tables S5 and S6) are presented in the Supporting Information. The best performing devices were obtained for a D:A ratio of 1:1.8, the total concentration of 10 mg mL^{-1} in chloroform and thermal treatment of the active layer at 100°C for 10 min for the donor polymer D18. Thus, further optimization and the corresponding device characterizations were done with D18.

The characteristic photovoltaic parameters of the best optimized devices and the respective current density–voltage (*J–V*) characteristics are reported in Table 2 and Figure 3a.

The solar cells with both material systems, D18:FHM-Cl and D18:FHM-F, exhibit comparable open-circuit voltage (V_{oc}) values (0.94–0.95 V), which is expected as the LUMO energy of both acceptors are very similar. In contrast, significant differences are observed in short-circuit current density (J_{sc}), fill factor (FF), and PCE. Notably, solar cells based on the D18:FHM-Cl blend, revealed the highest PCE of 10.69% with a FF of 0.76 and a J_{SC} of 15.15 mA cm^{-2}. Conversely, D18:FHM-F-based devices show lower J_{sc} (12.41 mA cm^{-2}) and FF (0.66), leading to a reduced PCE of 7.64%. This performance disparity correlates with the series resistance (R_s), which is substantially lower for FHM-Cl blends (3.08 Ω cm^2) compared to FHM-F (6.14 Ω cm^2), suggesting more efficient charge transport and reduced resistive losses in the former. EQE spectra were recorded to validate the variations in J_{sc} among the OPV devices (Figure 3b). Devices incorporating FHM-Cl exhibited a stronger EQE response across the total wavelength range, particularly above 70% in the range of 550–700 nm. The calculated J_{sc} values (J_{calc}) derived from the integration of the EQE spectra showed good agreement with the measured J_{sc}, having a mismatch of 3% and 5%, respectively.

The recombination properties of the D18:FHM-Cl and D18:FHM-F blends were studied by conducting *J–V* measurements at different light intensities (Figure 4 and Supporting Information 2.12). Since the J_{SC} increases monotonically with the incident light intensity (P_{in}) following the power law (Supporting Information 2.12, Equation 1), the experimental data were plotted in a double logarithmic scale and fitted to a linear regression (Figure 4a). The α factor is equal to 1 for both D18:FHM-Cl and D18:FHM blends, implying that at short circuit the bimolecular recombination is very weak. The ideality factor (n) is extrapolated from the relation

15213765, 0, Downloaded from https://chemistry-europe.onlinelibrary.wiley.com/doi/10.1002/chem.70952 by CochraneItalia, Wiley Online Library on [09/04/2026]. See the Terms and Conditions (https://onlinelibrary.wiley.com/terms-and-conditions) on Wiley Online Library for rules of use; OA articles are governed by the applicable Creative Commons License

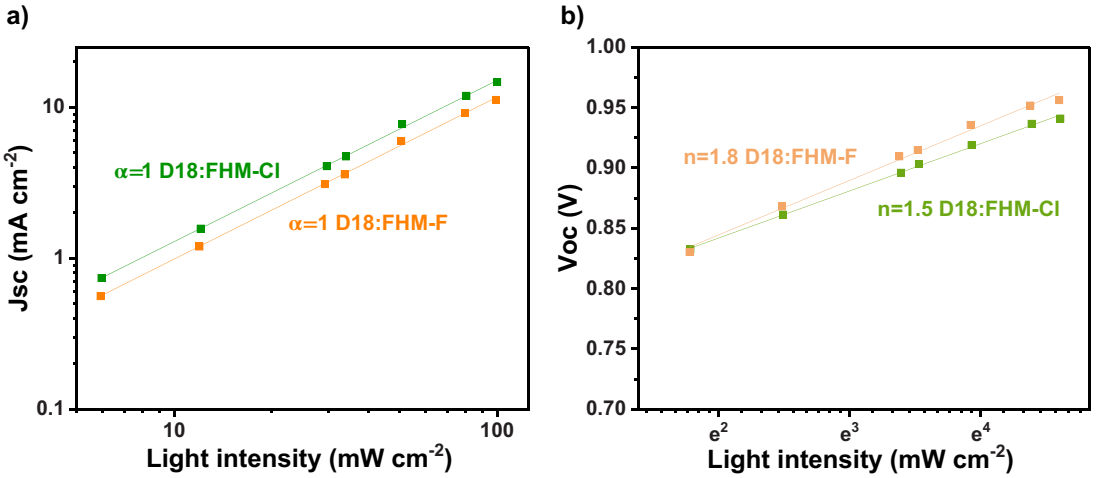

FIGURE 4 | Light intensity dependence measurements for D18:FHM-Cl (green) and D18:FHM-F (orange) solar cells: (a) J_{SC} and (b) V_{OC}.

between the V_{oc} and P_{in} (Figure 4b). When the value of n is 1 bimolecular recombination occurs while if it is 2, the system tends to be subjected to trap-assisted recombination. The ideality factor n is significantly higher in the fluorinated acceptor blend (1.8) than in the chlorinated counterpart (1.5), which suggests an increased trap-assisted recombination in this case.

Additionally, the electron (μ_e) and hole mobilities (μ_h) were determined by using the space-charge-limited current (SCLC) method (see Supporting Information 2.11). By fabricating electron and hole only devices, the mobility values can be deduced from the slope of the $J^{1/2}$ versus V following the Mott–Gurney law (Figure S20). The μ_e and μ_h values assessed for D18:FHM-Cl blend were 7.14×10^{-4} and 4.24×10^{-4} $cm^2V^{-1}s^{-1}$, respectively. In contrast, the D18:FHM-F devices exhibited significantly lower mobilities with μ_e and μ_h values of 1.14×10^{-5} and 3.15×10^{-5} $cm^2V^{-1}s^{-1}$, respectively, corresponding to approx. one order of magnitude reduction compared to the chlorinated counterpart. These reduced charge carrier mobilities indicate slower charge transport within the active layer, which increases the likelihood of recombination prior to charge extraction at the electrodes, consistent with the higher ideality factor observed for the FHM-F devices. Finally, to gain further insight into the exciton dissociation (η_{diss}) and charge collection efficiency (η_{coll}), the J_{ph}–V_{eff} characteristics were measured (see Supporting Information 2.13 and Figure S21). J_{sat} was extracted from the plateau region of the J_{ph}–V_{eff} characteristic curves ($J_{sat,FHM\text{-}Cl} = 16.0$ $mAcm^{-2}$, $J_{sat,FHM\text{-}F} = 13.8$ $mAcm^{-2}$). The D18:FHM-Cl and D18:FHM-F devices exhibit η_{diss} of 0.93 and 0.91, and η_{coll} of 0.80 and 0.70, respectively. These results indicate that a larger fraction of photogenerated charges in the fluorinated blend recombines before reaching the electrodes. Overall, the results suggest that the chlorinated acceptor material facilitates charge transport and suppressed charge recombination in the OPV devices, explaining the higher J_{SC} and FF values than those in devices fabricated with the fluorinated acceptor.

2.5 | Morphology Characterization

Given the performance difference between the devices based on D18:FHM-Cl and D18:FHM-F, we expected that the molecular packing and aggregation of neat and blend films would differ significantly within chlorinated and fluorinated acceptors. The investigation of the variations in material properties at the nanoscale was conducted with atomic force microscopy (AFM). Figure 5 shows the AFM images of D18:FHM-Cl and D18:FHM-F blend films characterized by the typical fibril like structure given by D18. The direct comparison of the topographic contrast (Figure 5a, b) shows only a slightly rougher surface morphology and a stronger phase contrast (Figure 5c, d) in D18:FHM-F than in D18:FHM-Cl blends with mean roughness values R of 1.67 and 1.46 nm, respectively. The phase contrast looks coarser in the case of the fluorinated material, which might be a cause of the difference in mobility.

The molecular stacking, orientation and the degree of crystallinity of the pristine acceptor materials and the blend films were investigated with 2D grazing-incidence wide-angle x-ray scattering (GIWAXS) measurements. The 2D GIWAXS patterns and the corresponding extracted 1D line cuts are shown in Figure 6, while the specific fitting results are presented in Tables S7, S8 and S9, for the neat FHM acceptors and D18:FHM-Cl and D18:FHM-F blends. The GIWAXS analysis of the neat acceptor films revealed that both FHM-Cl and FHM-F exhibit similar π–π stacking ($\approx$ 0.36 nm) and lamellar spacing ($\approx$1.52–1.54 nm), indicating minimal impact of the different halogenation on the packing distances.

A similar morphological behavior is evident in the blend films. In the out-of-plane (OOP) direction, the D18:FHM-Cl and D18:FHM-F films have similar π–π stacking peaks at 17.3 and 17.4 nm^{-1}, respectively, giving a d-spacing of 0.36 nm comparable to the pristine acceptors. From the fitting of the peaks in OOP direction, the D18:FHM-F sample reveals a narrower full width at half maximum (FWHM) with slightly longer crystalline coherence lengths (CCL) of 2.93 nm compared to 2.72 nm (D18:FHM-Cl).

Three lamellar stacking peaks at 3.1 and 5.4 nm^{-1} as well as at 4.1 nm^{-1}, corresponding to D18 and FHM features, respectively, are present in the in-plane (IP) direction for both blends. Upon blending, the lamellar stacking d-spacing gets marginally larger from 1.54 nm (FHM-Cl) to 1.57 nm (D18:FHM-Cl), and from 1.52 nm (FHM-F) to 1.53 nm (D18:FHM-F). While there is no

15213765, 0, Downloaded from https://chemistry-europe.onlinelibrary.wiley.com/doi/10.1002/chem.70952 by CochraneItalia, Wiley Online Library on [09/04/2026]. See the Terms and Conditions (https://onlinelibrary.wiley.com/terms-and-conditions) on Wiley Online Library for rules of use; OA articles are governed by the applicable Creative Commons License

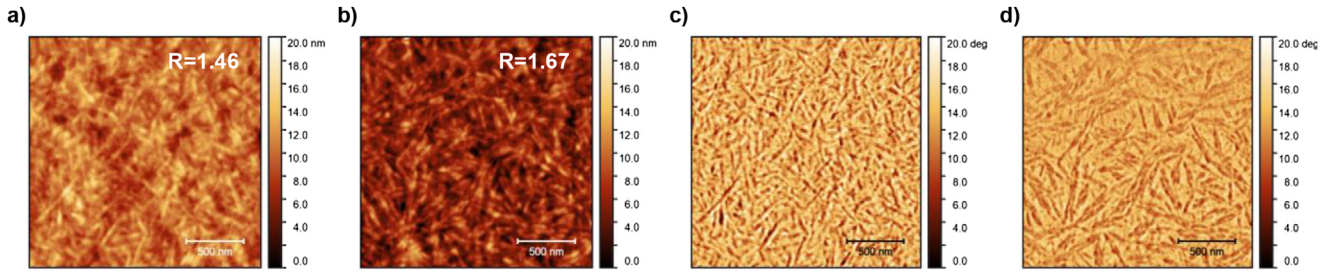

FIGURE 5 | Topographic (a and b, values in nm) and phase (c and d) AFM images of D18:FHM-Cl (a and c) and D18:FHM-F (b and d) films.

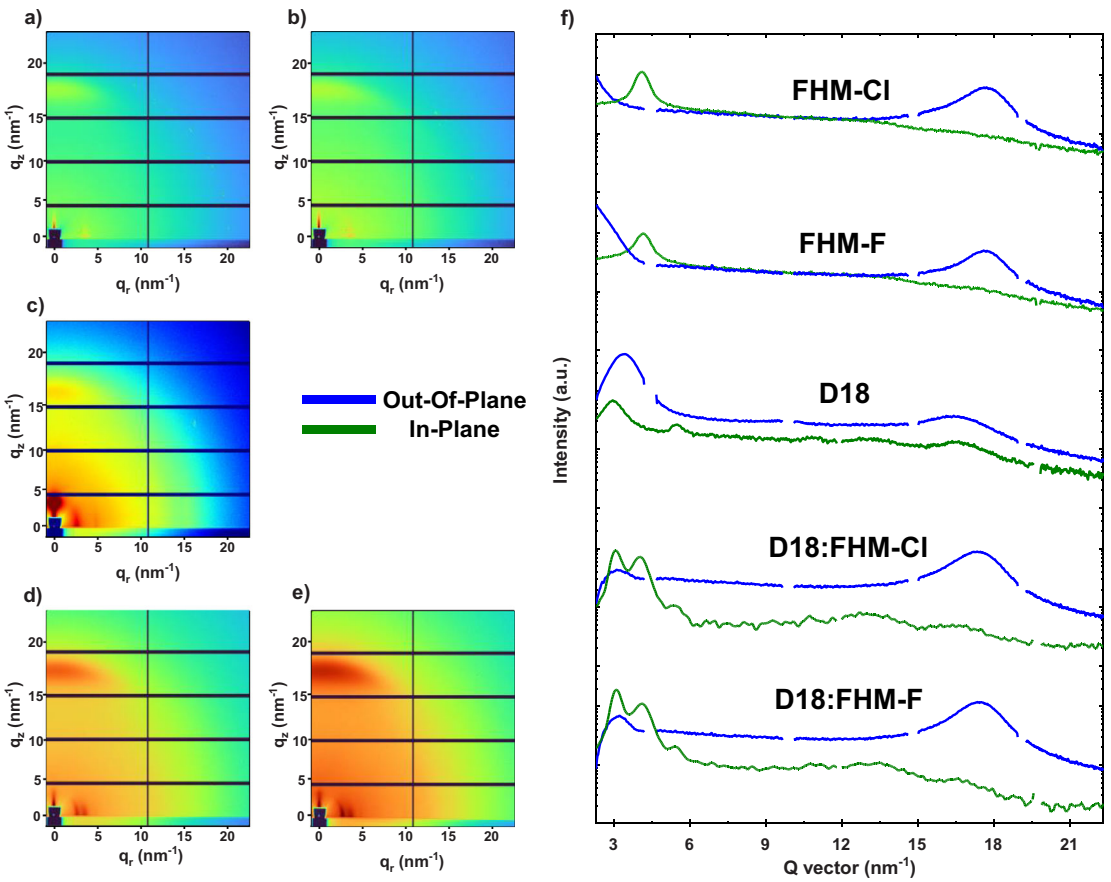

FIGURE 6 | 2D GIWAXS images of (a) FHM-Cl, (b) FHM-F, and (c) D18 neat films and (d) D18:FHM-Cl and (e) D18:FHM-F blend films; (f) corresponding out-of-plane (blue) and in-plane (green) line-cuts.

significant shift of the D18-IP peak at 5.4 nm^{-1}, the other D18-IP peak shifts from 3.0 nm^{-1} in the pristine polymer to 3.1 nm^{-1} in the blend, suggesting a similar to slightly more packed structure in presence of the acceptor. Notably, based on the IP peak at 4.1 nm^{-1}, D18:FHM-Cl shows a larger CCL (8.18 nm) than D18:FHM-F (5.88 nm), indicating enhanced lamellar ordering in D18:FHM-Cl (see Table S8).

2.6 | Device Stability

The storage and thermal stability of the optimized D18:FHM-F and D18:FHM-Cl devices were systematically evaluated. The devices were stored in a nitrogen-filled glove box, and their photovoltaic parameters were monitored periodically. As shown in Figure 7, both systems demonstrate good shelf-life stability, retaining performance for 950 h (D18:FHM-F: 85% of initial value; D18:FHM-Cl: 75% of initial value). For thermal stability testing, the devices were stored in the dark at 65 °C, and their performance evolution was recorded. The D18:FHM-Cl devices exhibited a typical burn-in loss within the first 12 h, but subsequently maintained 80% of their initial PCE after 500 h of aging. In contrast, D18:FHM-F devices showed a similar degradation trend to their shelf-stored counterparts (with hardly any burn in loss), with no significant additional decline during extended thermal stress, attributed to the reduced stacking d-spacing observed in the morphological characterization. The observed decrease in PCE is primarily driven by losses in FF (Figure 7b). Tracking of

15213765, 0, Downloaded from https://chemistry-europe.onlinelibrary.wiley.com/doi/10.1002/chem.70952 by CochraneItalia, Wiley Online Library on [09/04/2026]. See the Terms and Conditions (https://onlinelibrary.wiley.com/terms-and-conditions) on Wiley Online Library for rules of use; OA articles are governed by the applicable Creative Commons License

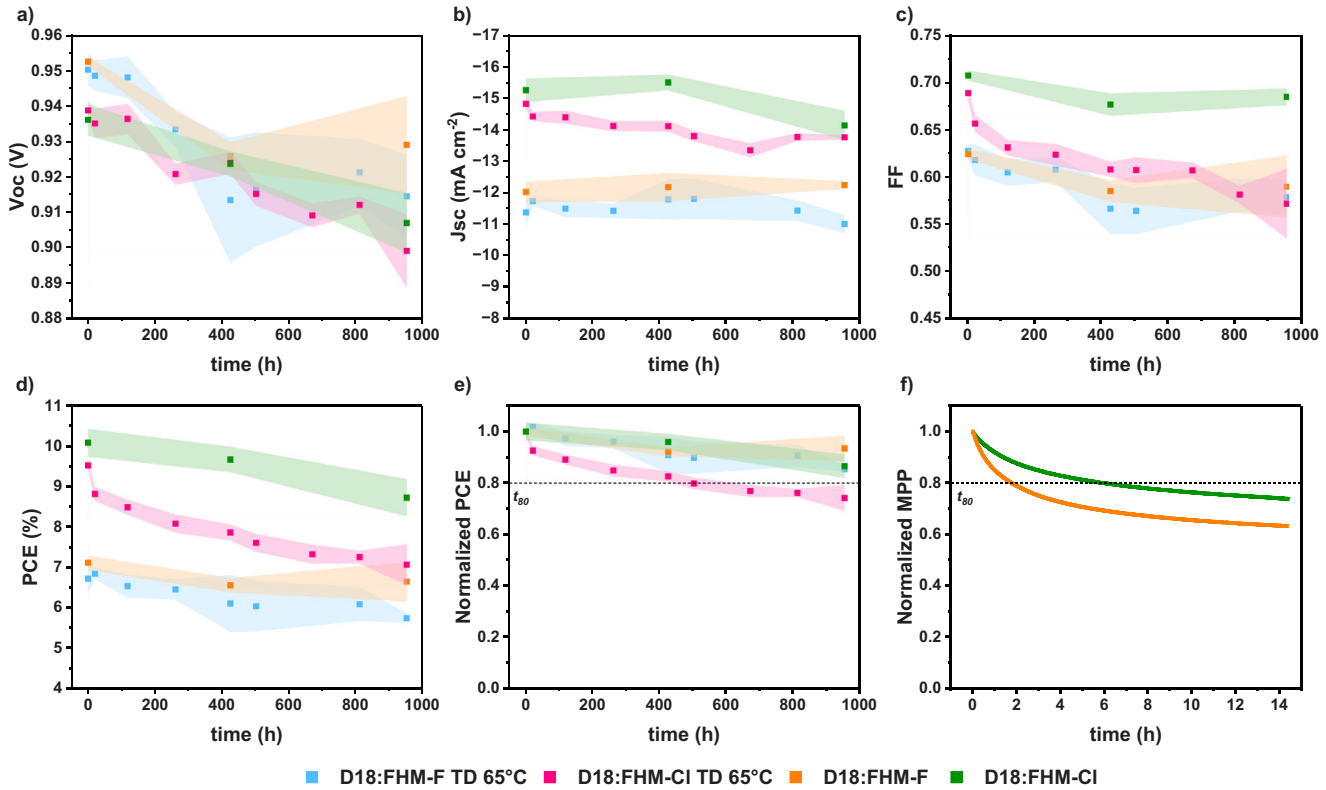

FIGURE 7 | Device storage stability (green and orange) and thermal stability (blue and pink) at 65°C and from an average of six devices; (a) V_{OC}; (b) J_{SC}; (c) FF; (d) PCE; (e) normalized PCE; and (f) normalized MPP tracking under 100 mW cm^{-2} illumination (green and organge).

the maximum power point (MPP) was conducted under 100 mW cm^{-2} illumination (Figure 7f). Interestingly, D18:FHM-Cl devices demonstrated a delayed degradation profile arising from a linear decay of the MPP current (I_{mpp}) (Figure S22), compared to a burn-in behavior of the D18:FHM-F devices.

3 | Conclusion

In summary, we have introduced two NFREAs, FHM-Cl and FHM-F, featuring a fluorene core, alkyl-substituted thiophene π-bridges, and chlorinated or fluorinated 1,1-dicyanomethylene-3-indanone end groups. Chlorination results in a red-shifted absorption relative to the fluorinated analogue, extending the light-harvesting range of the solar cells. Although both acceptors reveal the same LUMO level, FHM-Cl exhibits a higher HOMO energy level than FHM-F. Nevertheless, FHM-Cl shows a greater transfer integral and lower reorganization energy, consistent with its favorable packing observed in the pristine films, establishing it as the superior electron acceptor compared to FHM-F. When blended with the donor D18, the corresponding devices achieved PCEs of 10.7% (D18:FHM-Cl) and 7.6% (D18:FHM-F). Thus, the PCEs are lower than those of high efficient non-fused NFAs such as PTTz:EBO-4F [23] but among the highest reported for comparable fluorene based NFAs, see Table S10. The better performance of the chlorinated acceptor is attributed to enhanced charge generation and suppressed charge recombination, resulting in higher J_{SC} and FF values compared to the fluorinated counterpart. Furthermore, the higher charge carrier mobility in the D18:FHM-Cl blend facilitates efficient charge transport, thereby reducing recombination losses. It was also observed that substituting the fluorine atoms with chlorine on the end groups increases the surface tension difference and reduces donor–acceptor miscibility, leading to a higher degree of phase separation, as was confirmed by AFM investigations. Both devices exhibited good thermal stability, with FHM-F and FHM-Cl based devices showing respectively 15% and 25% efficiency loss after 950 h of prolonged thermal aging at 65°C. Owing to their favorable absorption profiles and wide bandgaps, these novel acceptor molecules show potential for application in indoor photovoltaic systems and in ternary device architectures.

4 | Experimental Section

The synthetic routes toward FHM-Cl and FHM-F and their characterizations as well as the full methodology regarding solar cell fabrication and characterization are included in the Supporting Information.

Acknowledgments

The authors acknowledge the OPVStability Project which has received funding from the European Union´s Horizon Europe MSCA-DN program under Grant Agreement Nr. 101120262, and the CERIC-ERIC Consortium for the financial support and access to experimental facilities of the Austrian SAXS beamline at Elettra Sincrotrone Trieste. The authors further thank Lukas Troi for the preparation of specific measurement setups as well as Hendrik Van Dooren and Kevin Pree for their experimental

15213765, 0, Downloaded from https://chemistry-europe.onlinelibrary.wiley.com/doi/10.1002/chem.70952 by CochraneItalia, Wiley Online Library on [09/04/2026]. See the Terms and Conditions (https://onlinelibrary.wiley.com/terms-and-conditions) on Wiley Online Library for rules of use; OA articles are governed by the applicable Creative Commons License

support. The authors appreciate the helpful comments and discussions provided by Safa Shoaee.

Open Access funding provided by Technische Universitat Graz/KEMO.

Conflicts of Interest

The authors declare no conflicts of interest.

Data Availability Statement

The data that support the findings of this study are openly available in Zenodo at http://doi.org/10.5281/zenodo.18866072.

References

1. E. N. Güler, A. Distler, R. Basu, C. J. Brabec, and H.-J. Egelhaaf, "Fully Solution-Processed, Light-Weight, and Ultraflexible Organic Solar Cells," *Flexible and Printed Electronics* 7 (2022): 25003, https://doi.org/10.1088/2058-8585/ac66ae.

2. X. Zhang, X. Wu, J. Zhang, et al., "Enhanced Charge Generation and Transport by Incorporating a Benzotriazole Unit for Low-Cost and High-Efficiency Organic Solar Cells," *ACS Nano* 19 (2025): 900–910, https://doi.org/10.1021/acsnano.4c12268.

3. R. Søndergaard, M. Hösel, D. Angmo, T. T. Larsen-Olsen, and F. C. Krebs, "Roll-to-Roll Fabrication of Polymer Solar Cells," *Materials Today* 15 (2012): 36–49, https://doi.org/10.1016/S1369-7021(12)70019-6.

4. J. Zhang, J. Zhong, S. Chung, et al., "π-Conjugation-Driven Aggregation Enhances Charge Transport in Y6 Derivatives for Bilayer Organic Solar Cells With 20% Efficiency," *Chemical Engineering Journal* 522 (2025): 167311, https://doi.org/10.1016/j.cej.2025.167311.

5. H. Chen, Y. Huang, R. Zhang, et al., "Organic Solar Cells With 20.82% Efficiency and High Tolerance of Active Layer Thickness Through Crystallization Sequence Manipulation," *Nature Materials* 24 (2025): 444–453, https://doi.org/10.1038/s41563-024-02062-0.

6. J. Fu, H. Li, H. Liu, et al., "Two-Step Crystallization Modulated Through Acenaphthene Enabling 21% Binary Organic Solar Cells and 83.2% Fill Factor," *Nature Energy* 10 (2025): 1251–1261, https://doi.org/10.1038/s41560-025-01862-1.

7. B. Schweda, M. Reinfelds, P. Hofstadler, G. Trimmel, and T. Rath, "Recent Progress in the Design of Fused-Ring Non-Fullerene Acceptors—Relations Between Molecular Structure and Optical, Electronic, and Photovoltaic Properties," *ACS Applied Energy Materials* 4 (2021): 11899–11981, https://doi.org/10.1021/acsaem.1c01737.

8. S. Dai, T. Li, W. Wang, et al., "Enhancing the Performance of Polymer Solar Cells via Core Engineering of NIR-Absorbing Electron Acceptors," *Advanced Materials* 30 (2018): e1706571, https://doi.org/10.1002/adma.201706571.

9. Y. Cui, H. Yao, J. Zhang, et al., "Single-Junction Organic Photovoltaic Cells With Approaching 18% Efficiency," *Advanced Materials* 32 (2020): e1908205, https://doi.org/10.1002/adma.201908205.

10. S. Feng, M. Li, N. Tang, et al., "Regulating the Packing of Non-Fullerene Acceptors via Multiple Noncovalent Interactions for Enhancing the Performance of Organic Solar Cells," *ACS Applied Materials & Interfaces* 12 (2020): 4638–4648, https://doi.org/10.1021/acsami.9b18076.

11. L. Ma, S. Zhang, J. Zhu, et al., "Completely Non-Fused Electron Acceptor With 3D-Interpenetrated Crystalline Structure Enables Efficient and Stable Organic Solar Cell," *Nature Communications* 12 (2021): 5093, https://doi.org/10.1038/s41467-021-25394-w.

12. R. Zeng, M. Zhang, X. Wang, et al., "Achieving 19% Efficiency in Non-Fused Ring Electron Acceptor Solar Cells via Solubility Control of Donor and Acceptor Crystallization," *Nature Energy* 9 (2024): 1117–1128, https://doi.org/10.1038/s41560-024-01564-0.

13. D. Luo, C. J. Brabec, and A. K. K. Kyaw, "Non-Fused Ring Electron Acceptors for High-Performance and Low-Cost Organic Solar Cells: Structure-Function, Stability and Synthesis Complexity Analysis," *Nano Energy* 114 (2023): 108661, https://doi.org/10.1016/j.nanoen.2023.108661.

14. Q. Bai, Q. Liang, H. Li, H. Sun, X. Guo, and L. Niu, "Recent Progress in Low-Cost Noncovalently Fused-Ring Electron Acceptors for Organic Solar Cells," *Aggregate* 3 (2022): e281, https://doi.org/10.1002/agt2.281.

15. M. Chen, Y. Zhang, J. Liu, Q. Wang, P. Song, and Y. Li, "Strategic Molecular Engineering of Non-Fused Non-Fullerene Acceptors: Efficiency Advances and Mechanistic Insight," *Chemical Science* 16 (2025): 14038–14080, https://doi.org/10.1039/d5sc00528k.

16. S. Shen, H. Lu, R. Zhu, et al., "Conformational Planarization Versus π–π Interacted Twisting: Precise Regulation of Chain Length for Rational Design of Nonfused Ring Electron Acceptors," *CCS Chemistry* 8 (2026): 1082–1093, https://doi.org/10.31635/ccschem.025.202505659.

17. N. Yang, Y. Cui, T. Zhang, et al., "Molecular Design of Fully Nonfused Acceptors for Efficient Organic Photovoltaic Cells," *Journal of the American Chemical Society* 146 (2024): 9205–9215, https://doi.org/10.1021/jacs.4c00090.

18. S. Ye, T. Chen, J. Yu, et al., "Enhanced Crystal Network and Charge Transfer of Non-Fused Ring Electron Acceptors via Interchain Interaction for Efficient and Stable Organic Solar Cells," *Energy & Environmental Science* 17 (2024): 5137–5146, https://doi.org/10.1039/D4EE02027H.

19. W. Zhang, K. Zhao, N. Zhang, et al., "Backbone Twisting and Terminal Overlapping via π-Bridge Engineering for Highly Efficient Non-Fused Ring Electron Acceptors With Balanced JSC—VOC," *Advanced Functional Materials* 35 (2025): 2423242, https://doi.org/10.1002/adfm.202423242.

20. X. Ding, X. Wu, S. Li, et al., "Constructing Efficient Fully Non-Fused Ring Electron Acceptor With Locked-In-Cavity Crystal Structure by Simple Polarized Design," *Advanced Functional Materials* 36 (2026): e11928, https://doi.org/10.1002/adfm.202511928.

21. S. Shen, Y. Mi, Y. Ouyang, et al., "Macrocyclic Encapsulation in a Non-Fused Tetrathiophene Acceptor for Efficient Organic Solar Cells With High Short-Circuit Current Density," *Angewandte Chemie* 62 (2023): e202316495, https://doi.org/10.1002/anie.202316495.

22. S. Shen, W. Liu, H. Lu, et al., "π-Extension Assisted Macrocycle-Encapsulated Non-Fused Ring Electron Acceptors With Dual Charge Transporting Pathways for High-Performance Organic Solar Cells," *Advanced Functional Materials* 35 (2025): 2507288, https://doi.org/10.1002/adfm.202507288.

23. Y. Wang, M. Yang, Z. Chen, et al., "Fully Non-Fused Electron Acceptor Solar Cells With 18% Efficiency via a Synergistic Peripheral Substituent Strategy," *Nature Communications* 16 (2025): 5449, https://doi.org/10.1038/s41467-025-60650-3.

24. K. Wang, Y. Firdaus, M. Babics, et al., "π-Bridge-Independent 2-(Benzo[c][1,2,5]thiadiazol-4-ylmethyleneMalononitrilee-Substituted Nonfullerene Acceptors for Efficient Bulk Heterojunction Solar Cells," *Chemistry of Materials* 28 (2016): 2200–2208, https://doi.org/10.1021/acs.chemmater.6b00131.

25. S. Holliday, R. S. Ashraf, C. B. Nielsen, et al., "A Rhodanine Flanked Nonfullerene Acceptor for Solution-Processed Organic Photovoltaics," *Journal of the American Chemical Society* 137 (2015): 898–904, https://doi.org/10.1021/ja5110602.

26. C.-H. Tan, J. Gorman, A. Wadsworth, et al., "Barbiturate End-Capped Non-Fullerene Acceptors for Organic Solar Cells: Tuning Acceptor Energetics to Suppress Geminate Recombination Losses," *Chemical Communications* 54 (2018): 2966–2969, https://doi.org/10.1039/c7cc09123k.

27. L. Zhang, S. Tu, W. Wang, and Q. Ling, "Brominated Small-Molecule Acceptors With a Simple Non-Fused Framework for Efficient Organic Solar Cells," *ACS Applied Energy Materials* 4 (2021): 4805–4814, https://doi.org/10.1021/acsaem.1c00369.

28. G. Li, M. Al-Hashimi, A. Facchetti, and T. J. Marks, "Decoding the Halogenation Cost-Performance Paradox in Organic Solar Cells," *Nature Reviews Materials* 10 (2025): 617–631, https://doi.org/10.1038/s41578-025-00804-3.

15213765, 0, Downloaded from https://chemistry-europe.onlinelibrary.wiley.com/doi/10.1002/chem.70952 by CochraneItalia, Wiley Online Library on [09/04/2026]. See the Terms and Conditions (https://onlinelibrary.wiley.com/terms-and-conditions) on Wiley Online Library for rules of use; OA articles are governed by the applicable Creative Commons License

29. J. Zhang, L. Wang, S. Wang, H. Gao, M. Xiao, and H. Song, "Impact of Molecular Engineering Strategies on the Packing Behavior and Photovoltaic Performance of Organic Solar Cells," *Materials Today Energy* 54 (2025): 102108, https://doi.org/10.1016/j.mtener.2025.102108.

30. C. Han, H. Gao, Y. Kan, et al., "Two Completely Non-Fused Ring Acceptors Working in an Alloy-Like Model for Efficient and Stable Organic Solar Cells," *Advanced Energy Materials* 14 (2024), https://doi.org/10.1002/aenm.202304063.

31. Q. Zhao, J. Qu, and F. He, "Chlorination: An Effective Strategy for High-Performance Organic Solar Cells," *Advanced Science* 7 (2020): 2000509, https://doi.org/10.1002/advs.202000509.

32. J. Shi, K. Sun, Z. Chen, et al., "The Influence of Donor/Acceptor Interfaces on Organic Solar Cells Efficiency and Stability Revealed Through Theoretical Calculations and Morphology Characterizations," *Angewandte Chemie International Edition in English* 63 (2024): e202318360, https://doi.org/10.1002/anie.202318360.

33. C. Park, S. Xuyao, G. Ham, et al., "Impact of Meta- and Para-Direction External Side Chains in Y-Series Acceptors on the Molecular Packing and Charge Carrier Dynamics of Organic Photovoltaics," *ACS Applied Materials & Interfaces* 17 (2025): 6648–6658, https://doi.org/10.1021/acsami.4c17649.

34. R. Ma, G. Li, D. Li, et al., "Understanding the Effect of End Group Halogenation in Tuning Miscibility and Morphology of High-Performance Small Molecular Acceptors," *Solar RRL* 4 (2020): 2000250, https://doi.org/10.1002/solr.202000250.

35. J. Zhang, W. Wei, Z. Luo, et al., "Halogenation-Engineered Acceptor Enables 20.14% Efficiency in Hydrocarbon-Solvent Processed OSCs: From Binary Trade-Offs to Ternary Synergy in Exciton and Energy Loss Management," *Angewandte Chemie International Edition in English* 64 (2025): e202512237, https://doi.org/10.1002/anie.202512237.

36. M. Li, Y. Liu, W. Ni, et al., "A Simple Small Molecule as an Acceptor for Fullerene-Free Organic Solar Cells With Efficiency Near 8%," *Journal of Materials Chemistry A* 4 (2016): 10409–10413, https://doi.org/10.1039/C6TA04358E.

37. H. J. Son, W. Wang, T. Xu, et al., "Synthesis of Fluorinated Polythienothiophene-Co-Benzodithiophenes and Effect of Fluorination on the Photovoltaic Properties," *Journal of the American Chemical Society* 133 (2011): 1885–1894, https://doi.org/10.1021/ja108601g.

38. A. Landi and D. Padula, "Multiple Charge Separation Pathways in New-Generation Non-Fullerene Acceptors: A Computational Study," *Journal of Materials Chemistry A* 9 (2021): 24849–24856, https://doi.org/10.1039/D1TA05664F.

39. B. Schlemmer, A. Sauermoser, S. Holler, et al., "Silicon- and Germanium-Functionalized Perylene Diimides: Synthesis, Optoelectronic Properties, and Their Application as Non-Fullerene Acceptors in Organic Solar Cells," *Chemistry- A European Journal* 29 (2023): e202301337, https://doi.org/10.1002/chem.202301337.

40. A. Kramer, R. Pachter, J. W. P. Hsu, and W. G. Vandenberghe, "The Effect of Solvent on Determining Highest Occupied Molecular Orbital Energies of Semiconducting Organic Molecules: Insight From a Combined Computational Approach," *Journal of Computational Chemistry* 44 (2023): 1064–1072, https://doi.org/10.1002/jcc.27065.

41. L. Ye, H. Hu, M. Ghasemi, et al., "Quantitative Relations Between Interaction Parameter, Miscibility and Function in Organic Solar Cells," *Nature Materials* 17 (2018): 253–260, https://doi.org/10.1038/s41563-017-0005-1.

42. D. Y. Kwok and A. W. Neumann, "Contact Angle Measurement and Contact Angle Interpretation," *Advances in Colloid and Interface Science* 81 (1999): 167–249, https://doi.org/10.1016/S0001-8686(98)00087-6.

43. S. Wu, "Calculation of Interfacial Tension in Polymer Systems," *Journal of Polymer Science Part C: Polymer Symposia* 34 (1971): 19–30, https://doi.org/10.1002/polc.5070340105.

44. L. Ma, S. Zhang, J. Ren, et al., "Design of a Fully Non-Fused Bulk Heterojunction Toward Efficient and Low-Cost Organic Photovoltaics," *Angewandte Chemie International Edition in English* 62 (2023): e202214088, https://doi.org/10.1002/anie.202214088.

45. C. M. Cardona, W. Li, A. E. Kaifer, D. Stockdale, and G. C. Bazan, "Electrochemical Considerations for Determining Absolute Frontier Orbital Energy Levels of Conjugated Polymers for Solar Cell Applications," *Advanced Materials* 23 (2011): 2367–2371, https://doi.org/10.1002/adma.201004554.

46. T. Nishinaga, *Organic Redox Systems*, (Wiley, 2016).

47. H. Amenitsch, M. Rappolt, M. Kriechbaum, H. Mio, P. Laggner, and S. Bernstorff, "First Performance Assessment of the Small-Angle X-ray Scattering Beamline at ELETTRA," *Journal of Synchrotron Radiation* 5 (1998): 506–508, https://doi.org/10.1107/S090904959800137X.

48. M. Burian, C. Meisenbichler, D. Naumenko, and H. Amenitsch, "SAXSDOG: Open Software for Real-Time Azimuthal Integration of 2D Scattering Images," *Journal of Applied Crystallography* 55 (2022): 677–685, https://doi.org/10.1107/S1600576722003685.

Supporting Information

Additional supporting information can be found online in the Supporting Information section.

Supplementary file 1: chem70952-sup-0001-SuppMat.pdf.

The authors have cited additional references within the Supporting Information [45–48].

15213765, 0, Downloaded from https://chemistry-europe.onlinelibrary.wiley.com/doi/10.1002/chem.70952 by CochraneItalia, Wiley Online Library on [09/04/2026]. See the Terms and Conditions (https://onlinelibrary.wiley.com/terms-and-conditions) on Wiley Online Library for rules of use; OA articles are governed by the applicable Creative Commons License